

Effect of synthesis methods on the $\text{Ca}_3\text{Co}_4\text{O}_9$ thermoelectric ceramic performances

A. Sotelo¹, Sh. Rasekh¹, M. A. Torres¹, P. Bosque², M. A. Madre^{1,*}, J. C. Diez¹

¹Instituto de Ciencia de Materiales de Aragón (CSIC-Universidad de Zaragoza), M^a de Luna, 3. 50018-Zaragoza, Spain.

²Centro Universitario de la Defensa de Zaragoza. Academia General Militar. Ctra. de Huesca s/n. 50090-Zaragoza, Spain.

Abstract

Three different synthesis methods producing nanometric grain sizes, coprecipitation with ammonium carbonate, oxalic acid, and by attrition milling have been studied to produce $\text{Ca}_3\text{Co}_4\text{O}_9$ ceramics and compared with the classical solid state route.

These three processes have produced high reactive precursors and all the organic material and CaCO_3 have been decomposed in a single thermal treatment.

Coprecipitation leads to pure $\text{Ca}_3\text{Co}_4\text{O}_9$ phase, while attrition milling and classical solid state produce small amounts of $\text{Ca}_3\text{Co}_2\text{O}_6$ secondary phase. Power factor values are similar for all three samples, being slightly lower for the ones produced by attrition milling. These values are much higher than the obtained in samples prepared by the classical solid state method, used as reference. The maximum power factor values determined at 800 °C ($\sim 0.43 \text{ mW/K}^2\text{m}$) are slightly higher than the best reported values obtained in textured ones which also show much higher density values.

Keywords: Ceramics; Synthesis; Electric properties; Microstructure; Power factor.

* Corresponding author: M. A. Madre

E-mail: amadre@unizar.es

Address: Dept. Ciencia de Materiales; C/M^a de Luna, 3; 50018-Zaragoza; Spain

Tel: +34 976762617

Fax: +34 976761957

1. Introduction

Thermoelectric (TE) power generation technology is regarded as one of the most promising methods to harvest energy from wasted and/or natural heat sources. In order to be used for practical applications, TE materials with high energy conversion efficiency are required for example, for electric power generation. Thermoelectric conversion is an effective technology that can be used to transform thermal to electrical energy. From this point of view, it can help to solve global warming by reducing CO₂ emissions improving the efficiency in classical energy transformation systems and exploiting natural heat sources. The conversion efficiency of TE materials is usually quantified by the dimensionless figure of merit ZT, which is defined as $TS^2/\rho\kappa$ (S^2/ρ is power factor, PF), where S is Seebeck coefficient, ρ electrical resistivity, κ thermal conductivity, and T absolute temperature [1]. From this expression, it is clear that a high performance TE material must possess high Seebeck coefficient together with low electrical resistivity and thermal conductivity. Semiconducting and intermetallic materials have been widely used to manufacture TE modules but, on the other hand, they are usually composed of heavy and/or toxic elements. Moreover, they can melt, evaporate or oxidize at high temperatures under air and these factors limit their range of applications. The discovery of high thermoelectric performances in a ceramic material, Na_xCoO₂ [2], provided a solution for these problems. This material is composed of non toxic and cheaper elements than the classical ones. Furthermore, it can operate at high temperatures, under air, for long time without degradation. As a consequence, the search for new oxide materials with high thermoelectric performances has been intensively performed. These efforts allowed the discovery of some other layered cobaltites, such as [Ca₂CoO₃][CoO₂]_{1.62} and [Bi_{0.87}SrO₂]₂[CoO₂]_{1.82} which were also extensively studied

due to their attractive thermoelectric properties [3-9]. Anyway, the TE properties nowadays reached must be increased before they can be used in practical applications [10].

The crystal structure of these CoO families is composed of two different layers, with an alternate stacking of a common conductive CdI₂-type CoO₂ layer with a two-dimensional triangular lattice and a block layer, composed of insulating rock-salt-type (RS) layers which lead to a very important crystalline and electrical anisotropy. Both sublattices (RS block and CdI₂-type CoO₂ layer) possess common a- and c-axis lattice parameters and β angles but different b-axis length, causing a misfit along the b-direction [11,12]. This anisotropy explains the great efforts put on the study and development of different texturing techniques which can produce polycrystalline materials with their ab planes parallel to the electrical transport direction. Some of them have already shown their potential in increasing the performances of ceramic TE materials, as sinter-forging [13], template grain growth [12], spark plasma texturing (SPT) [14], or directional growth from the melt [15]. In addition, different cation substitutions have been widely used to modify the bulk TE properties [16-20].

On the other hand, the preparation techniques have shown that they can influence drastically the bulk final properties [21], but synthesis methods have not yet been enough explored. Commonly, bulk materials are prepared following the classical solid state reaction method, which involves repeated mixing, milling and thermal treatments. Nevertheless, incomplete reaction, and compositional inhomogeneities are typical trademarks of conventional solid state reaction. In this context, other synthesis methods can offer several advantages, as higher precursor homogeneity and lower particle sizes which should lead to lower reaction times and/or

temperatures and/or higher performance materials. These characteristics, together with a high performances material, are of the main importance for their massive fabrication to be applied in power generation.

The aim of the present work is the study of different synthesis methods that yield small particle size and homogeneous precursors, to produce high-quality $\text{Ca}_3\text{Co}_4\text{O}_9$ bulk materials for practical applications. In this work it will be shown the comparison between three different synthesis methods which produce precursor powders with very high surface/volume relationship. These methods have already been used previously in other systems: coprecipitation with ammonium carbonate (as reported for LaGaO_3 in [22]), coprecipitation with oxalic acid (as reported for BaSnO_3 in [23]), and attrition milling (as reported for $\text{Bi}_2\text{Sr}_2\text{CaCu}_2\text{O}_x$ in [24]), using the solid state route as reference. A very important advantage of the two first methods is the intimate mixture of cations in the precipitate, which allows obtaining very pure final products. The final bulk properties will be determined, related with the microstructure, and compared with those obtained on classical solid state prepared samples.

2. Experimental

2.1. Synthesis

The initial $\text{Ca}_3\text{Co}_4\text{O}_9$ mixtures used in this work correspond to the appropriate amount of precursors to produce 5 g $\text{Ca}_3\text{Co}_4\text{O}_9$ in the coprecipitation methods while in the attrition and solid state procedures 20 g have been obtained due to the milling devices sizes. These products were prepared by the different methods described in detail in the following paragraphs:

(i) *Coprecipitation with ammonium carbonate* [22]: CaCO_3 ($\geq 99\%$, Aldrich), and $\text{Co}(\text{NO}_3)_2 \cdot 6\text{H}_2\text{O}$ ($\geq 99\%$, Aldrich) were dissolved in a mixture of HNO_3 (Fluka, PA) and distilled water. Once a clear solution was obtained, $(\text{NH}_4)_2\text{CO}_3$ (Panreac, PRS-CODEX) was added stepwise until a pH value of around 7.1 was obtained. This value has been determined experimentally as different pH values do not totally precipitate the different cations. The slurry was then kept at $75\text{ }^\circ\text{C}$ for 15 minutes with continuous stirring to age the precipitate. After this process, the resulting suspension was filtered to separate the solid product which was subsequently washed several times with distilled water. The light violet solid product was dried at $\sim 150\text{ }^\circ\text{C}$, calcined at $750\text{ }^\circ\text{C}$ for 12 h, manually milled, pressed at about 400 MPa in form of parallelepipeds ($\sim 3\text{ mm} \times 3\text{ mm} \times 14\text{ mm}$) and sintered at $900\text{ }^\circ\text{C}$ for 24 h with a final furnace cooling.

(ii) *Coprecipitation with oxalic acid* [23]: CaCO_3 ($\geq 99\%$, Aldrich), and $\text{Co}(\text{NO}_3)_2 \cdot 6\text{H}_2\text{O}$ ($\geq 99\%$, Aldrich) were dissolved in a mixture of HNO_3 (Fluka, PA) and distilled water. To the above clear solution, $\text{HOOC-COOH} \cdot 2\text{H}_2\text{O}$ (Panreac, $\geq 99.5\%$) was added stepwise until a pH value of around 0.4 was obtained. This value has been determined experimentally as different pH values do not totally precipitate the different cations. The resulting suspension was kept 15 minutes at $75\text{ }^\circ\text{C}$ with continuous stirring. The slurry was then filtered and washed several times with distilled water to isolate a light pink solid. The product was dried at $\sim 150\text{ }^\circ\text{C}$, calcined at $750\text{ }^\circ\text{C}$ for 12 h, manually milled, pressed at about 400 MPa in form of parallelepipeds ($\sim 3\text{ mm} \times 3\text{ mm} \times 14\text{ mm}$) and sintered at $900\text{ }^\circ\text{C}$ for 24 h with a final furnace cooling.

(iii) *Attrition milling* [24]: CaCO_3 ($\geq 99\%$, Aldrich), and Co_3O_4 (99.5%, Panreac) were mixed and attrition milled, using ZrO_2 balls as milling media in water, for 6 h. The

resulting slurry was then sieved and the balls were washed several times with distilled water to separate the grinding media and the milled solid. The suspension was then totally dried under infrared radiation until a soft brownish powder was obtained. The fine powder was calcined at 750 °C for 12 h, manually milled, pressed at about 400 MPa in form of parallelepipeds (~ 3 mm x 3 mm x 14 mm) and sintered at 900 °C for 24 h with a final furnace cooling.

(iv) *Classical solid state method* [25]: CaCO_3 ($\geq 99\%$, Aldrich), and Co_3O_4 (99.5%, Panreac) were mixed and ball milled, using agate balls as milling media in acetone, for 0.5 h. The resulting slurry was then sieved and the balls were washed several times with acetone to separate the grinding media and the milled solid. The suspension was then totally dried under infrared radiation until a soft brownish powder was obtained. The powder was then calcined twice at 750 °C and 800 °C for 12 h, with an intermediate manual milling, pressed at about 400 MPa in form of parallelepipeds (~ 3 mm x 3 mm x 14 mm) and sintered at 900 °C for 24 h with a final furnace cooling.

Hereafter, samples produced by the coprecipitation method with ammonium carbonate will be named S1, with oxalic acid, S2, the ones by attrition milling, S3, and the classical solid state ones, S4.

2.2. Characterization

The precursors evolution has been performed in several steps by DTA-TGA (TA Instruments, SDT Q600) between room temperature and 900 °C at a heating rate of 10 °C/min. FTIR (Bruker IFS 28 Spectrometer) has been used to identify the precipitate products, as well as the presence of CaCO_3 after the different thermal treatments. Moreover, the powders microstructure and grain size evolution has

been studied in a Field Emission Scanning Electron Microscope (FESEM, Carl Zeiss Merlin).

Phase identification in the sintered materials has been performed using powder X-ray diffraction (XRD) utilizing a Rigaku D/max-B X-ray powder diffractometer (CuK α radiation) with 2θ ranging between 10 and 70 degrees. Apparent density measurements have been performed on several samples for each synthesis method, as pressed and after sintering, using 4.677 g/cm³ as theoretical density [26]. Microstructural observations were performed on fractured and polished samples in a FESEM fitted with an energy dispersive spectrometry (EDS) device used to determine the elemental composition of each phase.

Oxygen content was determined in sintered materials by cerimetric titrations. In all cases, 100 ml HCl 1 N were kept under Ar flux during at least 1 h in order to evacuate the oxygen from the reaction vessel, avoiding the reactivities oxidation.

After this process, 50 mg of the powdered sample was added to the acidic solution to be dissolved, together with 100 mg FeCl₂ and a drop of ferroin indicator. In these solutions, Co⁺⁴ and Co⁺³ are reduced to Co⁺² while Fe⁺² is oxidized to Fe⁺³. Fe⁺³ is then titrated with a 0.015 M Ce(SO₄)₂ solution as described in previous works [21].

Electrical resistivity and Seebeck coefficient were simultaneously determined for samples obtained by the different synthesis methods, in steady state mode, by the standard dc four-probe technique in a LSR-3 apparatus (Linseis GmbH) between 50 and 800 °C under He atmosphere. With the electrical resistivity and Seebeck coefficient values, PF has been calculated to determine the TE performances.

3. Results and discussion

3.1. Precursors characterization

FTIR characterization has been performed on the dry precursors for the S1, S2, S3 and S4 samples and represented in Fig. 1. These study of the absorbance bands in the different spectra have shown the formation of Ca and Co(II) carbonates [27], with peaks at around 1470-1450 (strong), 1420-1400 (strong), and 880-860 (medium) cm^{-1} , in the S1 precursors promoted by the addition of $(\text{NH}_4)_2\text{CO}_3$ to the nitrates solution. In the S2 precursors the addition of oxalic acid has produced the Ca and Co(II) oxalates [27], with peaks at about 1620-1600 (strong), 1370-1350 (weak), 1330-1310 (medium), 840-820 (weak), and 790-770 (medium) cm^{-1} , while in the S3 and S4 ones, as they consist in a mixture of Ca carbonate and Co oxide, only CaCO_3 has been found [27], with its characteristic peaks found at around 1450-1400 (strong), and 880-860 (medium) cm^{-1} .

TGA measurements performed (under air) on the dry precursors for the S1, S2, S3 and S4 samples are presented in Fig. 2. As it can be clearly seen in the graph, the decomposition behaviour for the three first precursors is different, while it is very similar for the S3 and S4 ones. For the S1 precursors, the weight loss in the whole temperature range is about 36 % and it is produced in two steps, the first one starting at about 200 °C with (~ 16 % loss), due to the CoCO_3 decomposition, and the second one from around 600 °C (~ 14 %) due to the CaCO_3 decomposition. The S2 precursors show the highest weight loss of all of them due to their high proportion of organic material (due to the precipitated oxalates), as it has been described in the FTIR section. The decomposition of the dry precipitate has been produced in four steps, the first one starts at about 120 °C and it is probably due to water evaporation (~ 16 %), the second one starts at around 260 °C, associated to the Co oxalate decomposition to produce Co oxide, which is the sharpest and biggest one (~ 24 %). The third step is produced at 450 °C (~ 7 %), transforming the

Ca oxalate in Ca carbonate, and finally, the fourth step starts at 600 °C due to the CaCO_3 decomposition. The S3 and S4 precursors show the simplest decomposition path, as there is only one weight loss step, starting at about 600 °C, which is due to the CaCO_3 decomposition. On the other hand, both samples show a slight difference on the CaCO_3 decomposition starting temperature, slightly higher for the S4 samples due to their smaller surface area and lower reactivity, associated to the classical solid state method. Moreover, when observing the CaCO_3 decomposition temperature for all samples, it can be easily seen that this step is produced at the same temperature for the S1, S2, and S3 precursors, clearly confirming that the larger surface area decrease the CaCO_3 decomposition temperature.

DTA plots obtained in the same precursors are displayed in Fig. 3 where two different behaviours can be observed. S1, S3, and S4 precursors show very similar curves with a clear endothermic peak centered at around 700 °C and associated to the CaCO_3 decomposition. On the other hand, there are small differences between them which can be found in the broad and very small endothermic peaks centered at ~ 100 and ~250 °C, in the S1 precursors, which correspond to some water evaporation and to the CoCO_3 decomposition, respectively. Moreover, the S4 precursors shift the CaCO_3 decomposition to higher temperatures than the other ones, confirming the observations in the TGA analysis. The S2 precursors behave in a very different manner due to the high amount of organic material present in form of oxalates. They show a relatively intense endothermic peak at around 190 °C which can be associated to the evaporation of crystallization water. Moreover, two exothermic peaks, a very intense one at around 300 °C and a smaller one at about 490 °C, confirming the oxalates decomposition in two steps observed in the TGA

(see Fig. 2), can be found. Finally, at ~ 700 °C an endothermic peak is associated to the CaCO_3 decomposition, as it has been found for the S1 and S3 precursors.

In order to characterize the precursor powders obtained in the different synthesis methods, after the thermal treatment at 750 °C for 12 h, FTIR analysis has been performed in all the samples. The results are displayed in Fig. 4 where it can be clearly observed that S1, S2, and S3 precursors show the same spectra. Moreover, no absorption peaks of the most stable specie (CaCO_3) found in the system can be observed in these precursors, clearly indicating that most of it has been decomposed in the thermal treatment. As a consequence, it can be deduced that all these precursors are mainly composed of a mixture of CaO and CoO solid solutions. On the other hand, S4 precursors show different behaviour, associated to the presence of some CaCO_3 which has not been totally decomposed in this thermal treatment, confirming that the second thermal treatment at 800 °C is necessary in S4 samples.

In order to confirm that most of the carbonates have been decomposed in the thermal treatment at 700 °C, TGA analysis has been performed in all the precursors and the results are plotted in Fig. 5. In the graph, it is clear that the maximum weight loss corresponds to the S4 precursors (lower than 2.5 wt.%) while for the other precursors it is only around 1wt.%. These results are consistent with the presence of some CaCO_3 phase in the S4 samples, determined by FTIR.

FESEM images of the S1, S2, S3, and S4 precursor powders were recorded in order to observe their grain sizes and shapes, as the classical solid state samples possess much higher particle sizes. In Fig. 6, the representative images of the S1, S2, S3, and S4 calcined powders are shown. In the micrographs, it can be observed that S1 precursors are composed of approximately spherical aggregates

of about 500 nm which are, in turn, formed by smaller grains (typically < 100 nm, see Fig. 6a). On the other hand, S2 precursors are formed by very large grains (> 1 μm) with plate-like shape (see Fig. 6b). The shape and size of these grains can be explained by the high reactivity of the precipitated powders, which is increased with the energy produced by the selfcombustion of organic material present in these samples, as it was already discussed in the TGA and DTA analyses of the dry products. This high energy released promotes the rapid CaCO_3 decomposition, together with an increased reaction between CaO and CoO solid solutions to partially produce intermediate products. The S3 precursors are composed of a mixture of different sized grains, some ≤ 100 nm (#1 in Fig. 6c) while the others are ≥ 250 nm (#2 in Fig. 6c). These two different sizes are due to the different behaviour of CaCO_3 and CoO powders in the attrition milling process which lead to a different size reduction for each initial powder. Finally, S4 powders possess much bigger grain sizes (see Fig. 6d) than the observed for the other precursors due to the preparation method which is not greatly decreasing the initial grain sizes of commercial CaCO_3 and CoO.

3.2. Sintered materials characterization

Powder XRD plots for samples obtained for the different synthesis methods are represented (from 10 to 40 degrees for clarity) in Fig. 7. From the data represented in the figure it is very clear that all the samples show very similar patterns where the most intense peaks correspond to the crystallographic planes of the $\text{Ca}_3\text{Co}_4\text{O}_9$ phase [28], indexed in the plot. On the other hand, only small differences between the samples obtained by coprecipitation and the attrition and solid state ones have been found, and they are related to the presence of the peaks marked with a * in

Fig. 7d (associated to the $\text{Ca}_3\text{Co}_2\text{O}_6$ phase [28]) which are only in the S3 and S4 samples. This is a clear indication that, in the synthesis conditions used for the preparation of these samples, the use of the coprecipitation methods avoids the undesired $\text{Ca}_3\text{Co}_2\text{O}_6$ phase formation. This effect is probably due to the intimate mixture of the different cations in the initial powders produced by coprecipitation while in samples S3 and S4 this mixture is not produced. In any case, the $\text{Ca}_3\text{Co}_4\text{O}_9$ phase is the major one, independently of the synthesis route. On the other hand, cell parameters and volumes have been calculated using fullprof software using a C2/m space group and displayed in Table I. As it can be easily observed in the table, only slight differences can be found in the cell parameters, leading to nearly unchanged cell volumes in all cases. As a consequence, no structural changes are produced by the different synthesis methods.

SEM micrographs of representative transversal fractures for the different synthesis methods are displayed in Fig. 8. In these images it can be clearly observed that all the sintered samples show similar microstructures. They seem to be composed of randomly oriented plate-like grains with similar sizes for the S1, S2, and S3 methods, while they are much bigger for the S4 one, as can be observed in Table II where the mean grain sizes, together with their error, are displayed. On the other hand, careful observation of these micrographs shows that samples S1 and S2 possess higher grain size homogeneity than S3, and S4 ones, where grains larger than 2 μm coexist with very small ones ($< 100 \text{ nm}$, see Figs. 8c and d). This effect is probably due to the same factors discussed in the XRD paragraph, better cations mixture in the coprecipitation methods, leading to a relatively lower reactivity in samples S3 and S4 as a consequence of a larger distance between the different cations. In any case, the grain sizes observed for the S1, S2, and S3 methods are

much lower than the obtained through other solution or classical solid state routes [21]. Other feature that can be observed in the figure is the relatively large amount of porosity existing between the grains. In order to determine if this is a consequence of the samples preparation procedure or it is an inherent characteristic when sintered at the relatively low $\text{Ca}_3\text{Co}_4\text{O}_9$ stability temperatures, apparent density measurements have been performed on the ceramics obtained after sintering. Several samples from each synthesis method have been used in order to obtain accurate density values. The obtained values have been 3.45 ± 0.04 , 3.42 ± 0.04 , 3.47 ± 0.03 , and 3.44 ± 0.01 g/cm^3 for samples S1, S2, S3, and S4, respectively. These values correspond to densities between 73-74 % of the theoretical one for the $\text{Ca}_3\text{Co}_4\text{O}_9$ phase, indicating that the different porosity ratio observed in Fig. 8 is probably due to the low temperature used for the materials sintering and it is not really correlated with the bulk material. Moreover, measured densities for the sintered samples are higher than those reported in the literature for solid state sintered specimens (53-60 % of the theoretical one [29,30]) but lower than the obtained on samples processed by hot-pressing processes (92-96 % of the theoretical one [30,31]) which are characterized by their high density.

In order to confirm the observed random grain orientation in the different samples, out-of-plane XRD plots were performed on the surfaces. The obtained results are shown in Figure 9, where the representative patterns of the different synthesis methods are displayed. As it can be observed in the figure, main peaks correspond to the (00l) planes accompanied by small peaks associated to different grain orientations. This effect can be associated to the grains shape (plate-like one) which can order in the pressing procedure leading to a higher grain orientation in the surface than in the inner part. In any case, as it can be deduced for the graph,

the phenomenon is produced in all the samples and, as a consequence, its effect will be very similar in all samples.

Fig. 10 displays the variation of the Seebeck coefficient as a function of temperature for the three studied methods. All samples exhibit positive values in the whole studied temperature range, confirming a dominating hole conduction mechanism.

The obtained values are approximately the same for S1, S2, and S3 samples and to the typical ones reported in the literature ($\sim 125 \mu\text{V/K}$) at room temperature [32,33].

On the other hand, S4 samples show a slightly different behaviour, they possess higher Seebeck values from room temperature to $\sim 400 \text{ }^\circ\text{C}$ and lower at higher temperatures, compared to S1, S2, and S3 samples. The highest value at $800 \text{ }^\circ\text{C}$ ($\sim 235 \mu\text{V/K}$) for S1, S2, and S3 samples is considerably higher than the obtained in S4 ones ($\sim 205 \mu\text{V/K}$), in spark plasma sintered samples ($170\text{-}175 \mu\text{V/K}$) at about $625 \text{ }^\circ\text{C}$ [34], or laser floating zone ($\sim 205 \mu\text{V/K}$) at $800 \text{ }^\circ\text{C}$ [35].

The absolute oxygen content was determined on sintered samples using cerimetry titrations. For each sample four determinations were performed with each method, showing a reproducibility of around ± 0.008 in all cases. The obtained mean Co valence values are very similar for all samples and are around 3.130 ± 0.008 , being slightly lower for the S4 ones (displayed in Table III), in agreement with the higher room temperature Seebeck coefficient found in these samples [36]. On the other hand, these values should lead to room temperature Seebeck coefficients of about $300 \mu\text{V/K}$ when using Koshibae's expression [36]:

$$S = -\frac{k_B}{e} \ln\left(\frac{1}{6} x \frac{x}{1-x}\right)$$

where S is the Seebeck coefficient, k_B Boltzmann constant, e the absolute value of electron charge, and x the fraction of Co^{4+} . From this expression, it is clear that the raise in Co^{4+} content, decreases the Seebeck coefficient values.

The calculated value from Koshibae's expression is much higher than the experimental values found in this work while the mean Co valences determined in these samples agree with previously reported results on this material [37], indicating that only a low spin system model is not totally adequate to describe the global thermoelectric behaviour of this kind of materials.

The temperature (T) dependence of the electrical resistivity, as a function of the synthetic method, is shown in Fig. 11. As it can be easily seen, all the samples show very similar behaviour in all the measured temperature range, the $\rho(T)$ curve shows semiconducting-like behaviour ($d\rho/dT < 0$) under 400 °C, in agreement with previously reported data in this system where the charge transport process is a hole hopping from Co^{4+} to Co^{3+} [38]. At higher temperatures, the behaviour changes to a metallic-like ($d\rho/dT > 0$) one. On the other hand, S1, S2, and S3 samples possess much lower electrical resistivity than the S4 ones ($\sim 35\%$), slightly lower than the measured in samples prepared by solution methods (around 16 $\text{m}\Omega\cdot\text{cm}$) [21], or textured by a directional growth from the melt using the laser floating zone technique (about 15 $\text{m}\Omega\cdot\text{cm}$) [35], but still higher than the measured in SPT textured materials on the ab plane ($\sim 8 \text{ m}\Omega\cdot\text{cm}$) [30]. Furthermore, the electrical resistivity values determined in this work for samples S1, S2, and S3 can be found more impressive when taking into account that the best results reported in the literature have been obtained in samples with higher densities ($> 90\%$ of the theoretical density) than the ones produced in this work ($\sim 73\text{-}74\%$ of the theoretical one). The low electrical resistivity values obtained in these samples can be associated to the

formation of strong and clean grain boundaries due to the high reactivity of the different particles. This is in agreement with previous studies which showed that the electrical resistivity is more influenced by the number and strength of grain boundaries than for the amount of secondary phases in the structure [39].

From the electrical resistivity and Seebeck coefficient values, PF variation with temperature has been calculated for all the samples and represented in Fig. 12.

From this graph, it is clear that S1, S2, and S3 samples possess very similar PF values, except in the high temperature range, where S3 show a slightly lower PF than the obtained in the other two. On the other hand, S4 ones possess much lower PF in all the measured temperature range. The maximum PF value at 800 °C ($\sim 0.43 \text{ mW/K}^2 \cdot \text{m}$) obtained for samples S1 and S2 is about 10 and 110 % higher than the measured in S3 and S4 samples, respectively. Moreover, it is around those measured on textured materials produced by spark plasma texturing (SPT) technique ($\sim 0.40 \text{ mW/K}^2 \cdot \text{m}$ at 550 °C) [14], or laser floating zone technique [35]. Furthermore, this high PF value is again more impressive when considering the relative density of the samples, between 73-74 % of the theoretical one, while for the spark plasma or laser floating zone prepared samples, the densities easily exceed 90 %.

These high PF values obtained with relatively economic and scalable preparation techniques make these sintered materials promising candidates for practical applications in high temperature thermoelectric devices.

4. Conclusions

A comparison of several synthetic routes for obtaining the $\text{Ca}_3\text{Co}_4\text{O}_9$ phase, coprecipitation with ammonium carbonate or oxalic acid, attrition milling, and

classical solid state method, has been made. All coprecipitation and attrition milling methods have produced very reactive precursors, reflected in the whole CaCO_3 decomposition after only a thermal treatment at 750 °C for 12 h. The attrition milling and the classical solid state methods result in nearly single $\text{Ca}_3\text{Co}_4\text{O}_9$ phase with very small amounts of $\text{Ca}_3\text{Co}_2\text{O}_6$ one while the coprecipitation methods evaluated in this study produce pure $\text{Ca}_3\text{Co}_4\text{O}_9$ phase. The thermoelectric performances have shown to be dependent of the precursors homogeneity and initial grain sizes, leading to PF values for the attrition and coprecipitation methods of around two times higher than the obtained for the classical solid state method ones. Moreover, in spite of the relatively low density of the samples prepared in this work, their highest PF values at 800 °C are slightly higher than the best values obtained on high-density textured $\text{Ca}_3\text{Co}_4\text{O}_9$ materials reported in the literature.

Acknowledgements

The authors wish to thank the Gobierno de Aragón (Grupos de Investigación Consolidados T12 and T87) and MINECO-FEDER (MAT2013-46505-C3-1-R) for financial support, and to Prof. J.-P. Habas and A. Ulloa-Habas from the Institute Charles Gerhardt (Univ. Montpellier 2) for their help on the FTIR characterizations. Authors would like to acknowledge the use of Servicio General de Apoyo a la Investigación-SAI, Universidad de Zaragoza. Sh. Rasekh acknowledges a JAEPredoc2010 grant from the CSIC.

References

1. Rowe DM (2006) In: Rowe DM (ed.), Thermoelectrics Handbook: Macro to Nano, 1st edn. CRC Press, Boca Raton, FL.
2. Terasaki I, Sasago Y, Uchinokura K. Large thermoelectric power in NaCo_2O_4 single crystals. *Phys Rev B* 56, 12685-12687 (1997)
3. Diez JC, Guilmeau E, Madre MA, Marinel S, Lemonnier S, Sotelo A. Improvement of $\text{Bi}_2\text{Sr}_2\text{Co}_{1.8}\text{O}_x$ thermoelectric properties by laser floating zone texturing. *Solid State Ionics* 180, 827-830 (2009)
4. Masset AC, Michel C, Maignan A, Hervieu M, Toulemonde O, Studer F, Raveau B, Hejtmanek J. Misfit-layered cobaltite with an anisotropic giant magnetoresistance: $\text{Ca}_3\text{Co}_4\text{O}_9$. *Phys Rev B* 62, 166-175 (2000)
5. Sotelo A, Rasekh Sh, Madre MA, Guilmeau E, Marinel S, Diez JC. Solution-based synthesis routes to thermoelectric $\text{Bi}_2\text{Ca}_2\text{Co}_{1.7}\text{O}_x$. *J Eur Ceram Soc* 31, 1763-1769 (2011)
6. Maignan A, Pelloquin D, Hébert S, Klein Y, Hervieu M. Thermoelectric power in misfit cobaltites ceramics: Optimization by chemical substitutions. *Bol Soc Esp Ceram V* 45, 122-125 (2006)
7. Funahashi R, Matsubara I, Ikuta H, Takeuchi T, Mizutani U, Sodeoka S. An Oxide Single Crystal with High Thermoelectric Performance in Air. *Jpn. J. Appl. Phys.* 39, L1127-L1129 (2000)
8. Funahashi R, Matsubara I. Thermoelectric Properties of Pb- and Ca-doped $(\text{Bi}_2\text{Sr}_2\text{O}_4)_x\text{CoO}_2$ Whiskers. *Appl. Phys. Lett.* 79, 362-364 (2001)
9. Koumoto K, Funahashi R, Guilmeau E, Miyazaki Y, Weidenkaff A, Wang Y, Wan C. Thermoelectric Ceramics for Energy Harvesting, *J. Am. Ceram. Soc.* 96, 1-23 (2013)

10. Koumoto K, Terasaki I, Funahashi R. Complex Oxide Materials for Potential Thermoelectric Applications. MRS Bulletin, 31, 206-210 (2006)
11. Maignan A, Hébert S, Hervieu M, Michel C, Pelloquin D, Khomskii D. Magnetoresistance and magnetothermopower properties of Bi/Ca/Co/O and Bi(Pb)/Ca/Co/O misfit layer cobaltites. J Phys: Condens Matter 15, 2711-2723 (2003)
12. Itahara H, Xia C, Sugiyama J, Tani T. Fabrication of textured thermoelectric layered cobaltites with various rock salt-type layers by using β -Co(OH)₂ platelets as reactive templates, J Mater Chem 14, 61-66 (2004)
13. Fukutomi H, Konno Y, Okayasu K, Hasegawa M, Nakatsugawa H. Texture development of Ca₃Co₄O₉ thermoelectric oxide by high temperature plastic deformation and its contribution to the improvement in electric conductivity. Mater Sci Eng A 527, 61-64 (2009)
14. Noudem JG, Kenfaui D, Chateigner D, Gomina M. Toward the enhancement of thermoelectric properties of lamellar Ca₃Co₄O₉ by edge-free spark plasma texturing. Scripta Mater 66, 258-260 (2012)
15. Sotelo A, Guilmeau E, Madre MA, Marinel S, Diez JC, Prevel M. Fabrication and properties of textured Bi-based cobaltite thermoelectric rods by zone melting. J Eur Ceram Soc 27, 3697-3700 (2007)
16. Sotelo A, Rasekh Sh, Guilmeau E, Madre MA, Torres MA, Marinel S, Diez JC. Improved thermoelectric properties in directionally grown Bi₂Sr₂Co_{1.8}O_y ceramics by Pb for Bi substitution. Mater Res Bull 46, 2537-2542 (2011)
17. Sun N, Dong ST, Zhang BB, Chen YB, Zhou J, Zhang ST, Gu ZB, Yao SH, Chen YF. Intrinsically modified thermoelectric performance of alkaline-earth

isovalently substituted $[\text{Bi}_2\text{AE}_2\text{O}_4][\text{CoO}_2]_y$ single crystals. *J Appl Phys* 114, 043705 (2013)

18. Sotelo A, Torres MA, Constantinescu G, Rasekh Sh, Diez JC, Madre MA. Effect of Ag addition on the mechanical and thermoelectric performances of annealed $\text{Bi}_2\text{Sr}_2\text{Co}_{1.8}\text{O}_x$ textured ceramics. *J Eur Ceram Soc* 32, 3745-3751 (2012)

19. Demirel S, Aksan MA, Altin S. Low temperature electrical and thermal transport properties of the $\text{Ca}_{3-x}\text{Sb}_x\text{Co}_4\text{O}_9$ system. *J Mater Sci: Mater Electron* 23, 2251-2256 (2012)

20. Sotelo A, Rasekh Sh, Constantinescu G, Torres MA, Madre MA, Diez JC. Improvement of textured $\text{Bi}_{1.6}\text{Pb}_{0.4}\text{Sr}_2\text{Co}_{1.8}\text{O}_x$ thermoelectric performances by metallic Ag additions. *Ceram Int* 39, 1597-1602 (2013)

21. Sotelo A, Constantinescu G, Rasekh Sh, Torres MA, Diez JC, Madre MA. Improvement of thermoelectric properties of $\text{Ca}_3\text{Co}_4\text{O}_9$ using soft chemistry synthetic methods. *J Eur Ceram Soc* 32, 2415-2422 (2012)

22. Chae N S, Park K S, Yoon Y S, Yoo I S, Kim J S, Yoon H H. Sr- and Mg-doped LaGaO_3 powder synthesis by carbonate coprecipitation. *Colloid. Surface. A* 313-314, 154-157 (2008)

23. Song Y J, Kim S. Preparation of fine BaSnO_3 powders by oxalate coprecipitation method. *J. Ind. Eng. Chem.* 7, 183-185 (2001)

24. Garnier V, Caillard R, Sotelo A, Desgardin G. Relationship among synthesis, microstructure and properties in sinter-forged Bi-2212 ceramics. *Physica C* 319, 197-208 (1999)

25. Rasekh Sh, Torres MA, Constantinescu G, Madre MA, Diez JC, Sotelo A. Effect of Cu by Co substitution on $\text{Ca}_3\text{Co}_4\text{O}_9$ thermoelectric ceramics. *J Mater Sci: Mater Electron* 24, 2309-2314 (2013)

26. Diez JC, Torres MA, Rasekh Sh, Constantinescu G, Madre MA, Sotelo A. Enhancement of $\text{Ca}_3\text{Co}_4\text{O}_9$ thermoelectric properties by Cr for Co substitution. *Ceram Int* 39, 6051-6056 (2013)
27. Chemistry WebBook of NIST. <http://webbook.nist.gov/chemistry/>
28. Woermann E, Muan A. Phase equilibria in the system CaO-cobalt oxide in air. *J Inorg Nucl Chem* 32, 1455-1459 (1970)
29. Liou YC, Tsai WC, Lin WY, Lee UR. Synthesis of $\text{Ca}_3\text{Co}_4\text{O}_9$ and CuAlO_2 ceramics of the thermoelectric application using a reaction-sintering process. *J Aust Ceram Soc* 44, 17-22 (2008)
30. Kenfaui D, Lenoir B, Chateigner D, Ouladdiaf B, Gomina M, Noudem JG. Development of multilayer textured $\text{Ca}_3\text{Co}_4\text{O}_9$ materials for thermoelectric generators: Influence of the anisotropy on the transport properties. *J Eur Ceram Soc* 32, 2405-2414 (2012)
31. Wang H, Sun X, Yan X, Huo D, Li X, Li J-G, Ding X. Fabrication and thermoelectric properties of highly textured $\text{Ca}_9\text{Co}_{12}\text{O}_{28}$ ceramic. *J Alloys Compd* 582, 294-298 (2014)
32. Wang Y, Sui Y, Wang X, Su W, Liu X. Enhanced high temperature thermoelectric characteristics of transition metals doped $\text{Ca}_3\text{Co}_4\text{O}_{9+\delta}$ by cold high-pressure fabrication. *J Appl Phys* 107, 033708 (2010)
33. Liu HQ, Zhao XB, Zhu TJ, Song Y, Wang FP. Thermoelectric properties of Gd, Y co-doped $\text{Ca}_3\text{Co}_4\text{O}_{9+\delta}$. *Current Appl Phys* 9, 409-413 (2009)
34. Kenfaui D, Bonnefont G, Chateigner D, Fantozzi G, Gomina M, Noudem JG. $\text{Ca}_3\text{Co}_4\text{O}_9$ ceramics consolidated by SPS process: Optimisation of mechanical and thermoelectric properties. *Mater Res Bull* 45, 1240-1249 (2010)

35. Madre MA, Costa FM, Ferreira NM, Sotelo A, Torres MA, Constantinescu G, Rasekh Sh, Diez JC. Preparation of high-performance $\text{Ca}_3\text{Co}_4\text{O}_9$ thermoelectric ceramics produced by a new two-step method. *J Eur Ceram Soc* 33, 1747-1754 (2013)
36. Koshibae W, Tsutsui K, Maekawa S. Thermopower in cobalt oxides. *Phys Rev B* 62, 6869-6872 (2000)
37. Karppinen M, Fjellvåg H, Konno T, Morita Y, Motohashi T, Yamauchi H. Evidence for oxygen vacancies in misfit-layered calcium cobalt oxide, $[\text{CoCaO}]\text{CoO}$. *Chem Mater* 16, 2790-2793 (2004)
38. Lin YH, Lan J, Shen ZJ, Liu YH, Nan CW, Li JF. High-temperature electrical transport behaviors in textured $\text{Ca}_3\text{Co}_4\text{O}_9$ -based polycrystalline ceramics. *Appl Phys Lett* 94, 072107 (2009)
39. Rasekh Sh, Constantinescu G, Madre MA, Torres MA, Diez JC, Sotelo A. Processing effects on the thermoelectric properties of $\text{Bi}_2\text{Ca}_2\text{Co}_{1.7}\text{O}_x$ ceramics. *Bol Soc Esp Ceram V* 2014. DOI: 10.3989/cyv.xx2014

Table I. Cell parameters and volumes obtained with fullprof for the different synthesis methods

Sample	a	b	c	β	Volume
Coprecipitation [(NH₄)₂CO₃]	4.8361(6)	4.5520(9)	10.8020(1)	98.46(1)	235.20(5)
Coprecipitation [HOCCOOH]	4.8344(6)	4.5522(8)	10.8051(9)	98.44(1)	235.21(6)
Attrition milling	4.8133(5)	4.5425(8)	10.8159(9)	98.43(2)	235.38(7)
Classical solid state	4.8327(6)	4.5549(9)	10.8110(1)	98.17(1)	235.60(5)

Table II. Mean grain sizes, together with their errors, for sintered samples prepared by the different methods

Sample	Mean grain size (μm)	Error
Coprecipitation [(NH₄)₂CO₃]	1.48	0.12
Coprecipitation [HOCCOOH]	1.30	0.16
Attrition milling	1.07	0.05
Classical solid state	3.16	0.22

Table III. Mean Co valences, together with their errors, for the samples prepared by the different methods

Sample	Mean Co valence	Error
Coprecipitation [(NH₄)₂CO₃]	3.128	0.008
Coprecipitation [HOCCOOH]	3.129	0.008
Attrition milling	3.133	0.008
Classical solid state	3.112	0.006

Figure captions

Figure 1. FTIR spectra of the dry products obtained by the (-■-) S1; (-●-) S2; (-▲-) S3; and (-▼-) S4 methods.

Figure 2. TGA plots vs. temperature of the dry products obtained by the (-■-) S1; (-●-) S2; (-▲-) S3; and (-▼-) S4 methods.

Figure 3. DTA plots vs. temperature of the dry products obtained by the (-■-) S1; (-●-) S2; (-▲-) S3; and (-▼-) S4 methods.

Figure 4. FTIR spectra of the different precursors after the thermal treatment at 750 °C for 12 h. (-■-) S1; (-●-) S2; (-▲-) S3; and (-▼-) S4 methods.

Figure 5. TGA plots vs. temperature of the calcined powders obtained by the (-■-) S1; (-●-) S2; (-▲-) S3; and (-▼-) S4 methods.

Figure 6. FESEM micrographs obtained in the calcined powders obtained by S1 (a); S2 (b); S3 (c); and S4 (d) methods. #1 indicates the small particles (≤ 100 nm); #2 shows the big ones (≥ 250 nm).

Figure 7. XRD plots of the $\text{Ca}_3\text{Co}_4\text{O}_9$ sintered specimens obtained for the different synthetic methods. a) S1; b) S2; c) S3, and d) S4. Crystallographic planes indicate the peaks for the $\text{Ca}_3\text{Co}_4\text{O}_9$ phase and the * shows those belonging to the $\text{Ca}_3\text{Co}_2\text{O}_6$ one.

Figure 8. Scanning electron micrographs obtained on transversal fractured $\text{Ca}_3\text{Co}_4\text{O}_9$ samples prepared by the different synthesis methods: (a) S1; (b) S2; (c) S3; and (d) S4.

Figure 9. Out-of-plane XRD plots obtained in samples prepared by different synthesis methods: (a) S1; (b) S3; and (c) S4.

Figure 10. Temperature dependence of the Seebeck coefficient for $\text{Ca}_3\text{Co}_4\text{O}_9$, as a function of the synthesis method. (-■-) S1; (-●-) S2; (-▲-) S3; and (-▼-) S4.

Figure 11. Temperature dependence of the electrical resistivity for $\text{Ca}_3\text{Co}_4\text{O}_9$, as a function of the synthesis method. (-■-) S1; (-●-) S2; (-▲-) S3; and (-▼-) S4.

Figure 12. Temperature dependence of the power factor for $\text{Ca}_3\text{Co}_4\text{O}_9$, as a function of the synthesis method. (-■-) S1; (-●-) S2; (-▲-) S3; and (-▼-) S4.

Figure 1

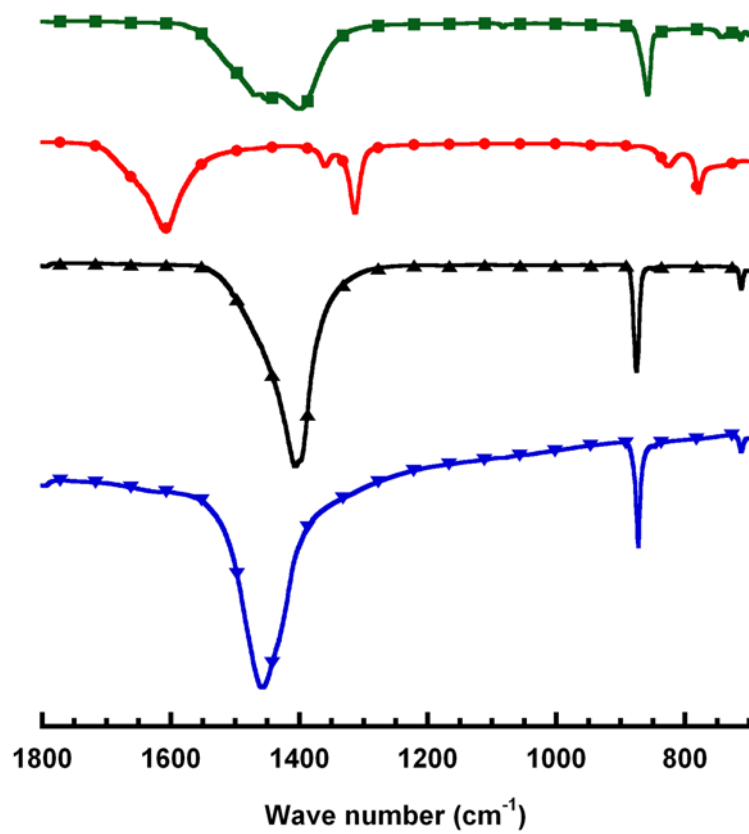


Figure 2

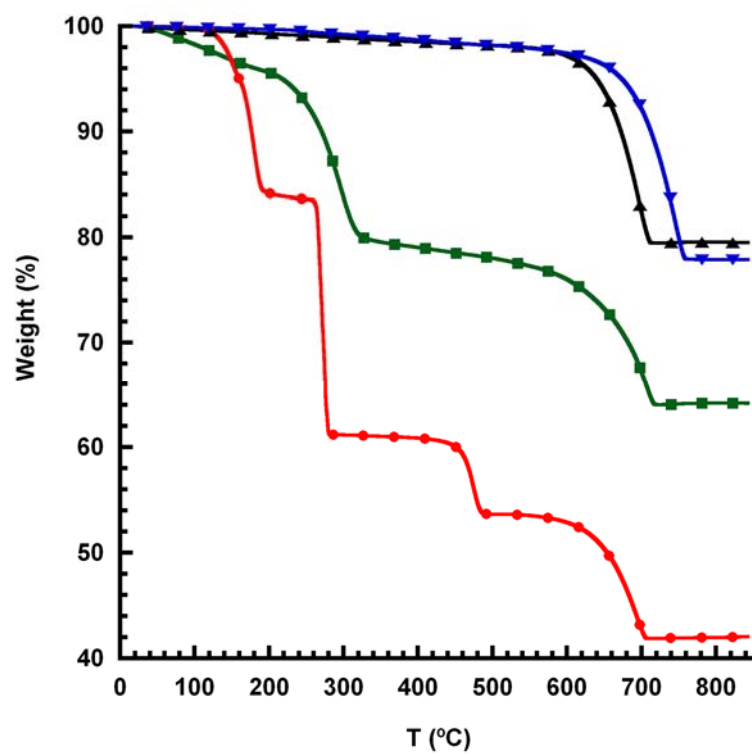


Figure 3

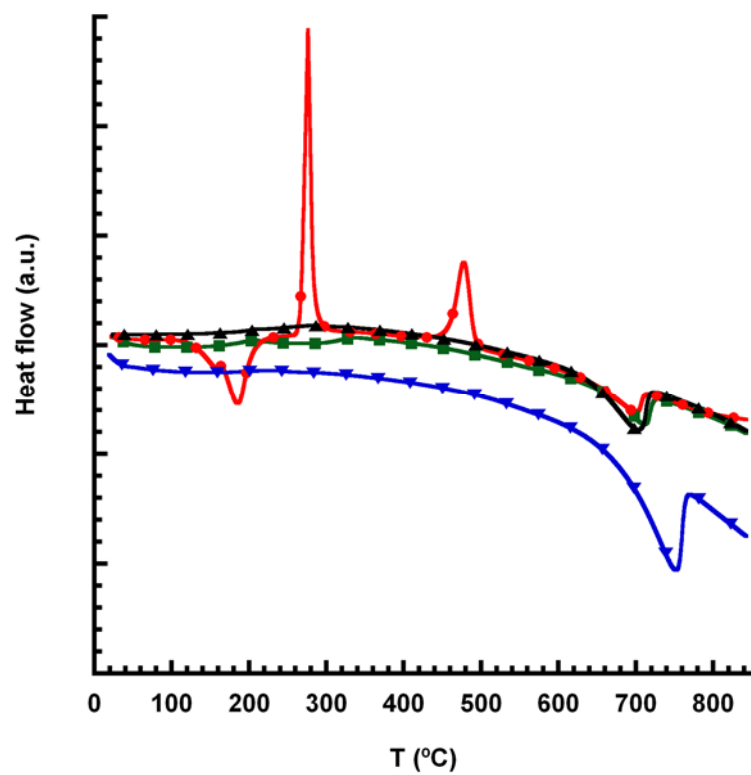


Figure 4

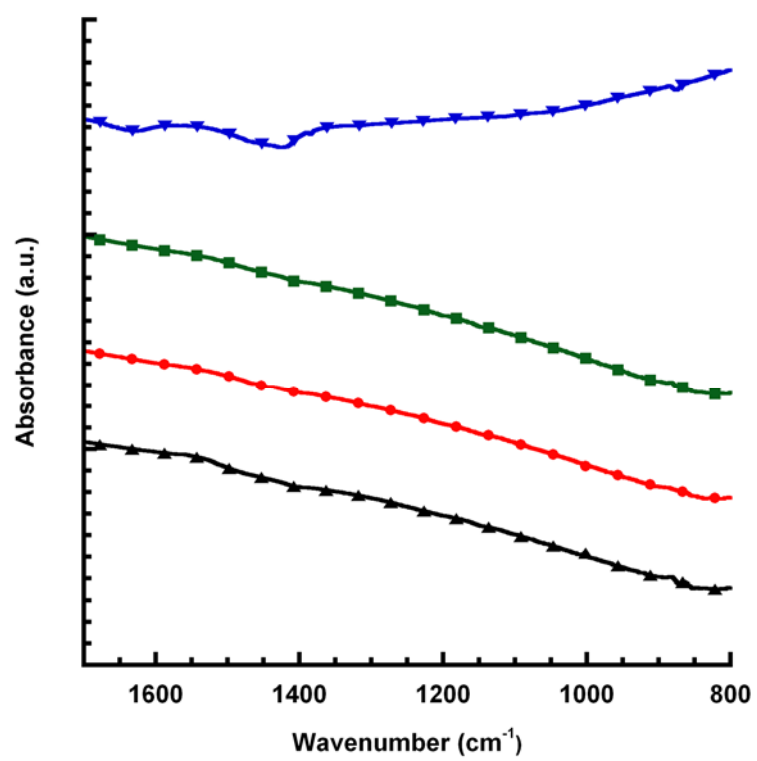


Figure 5

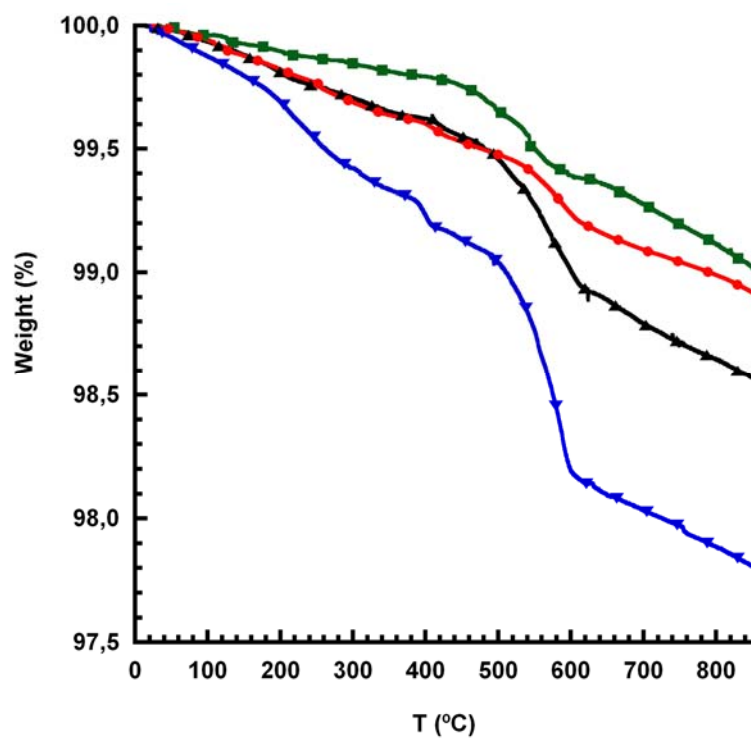


Figure 6

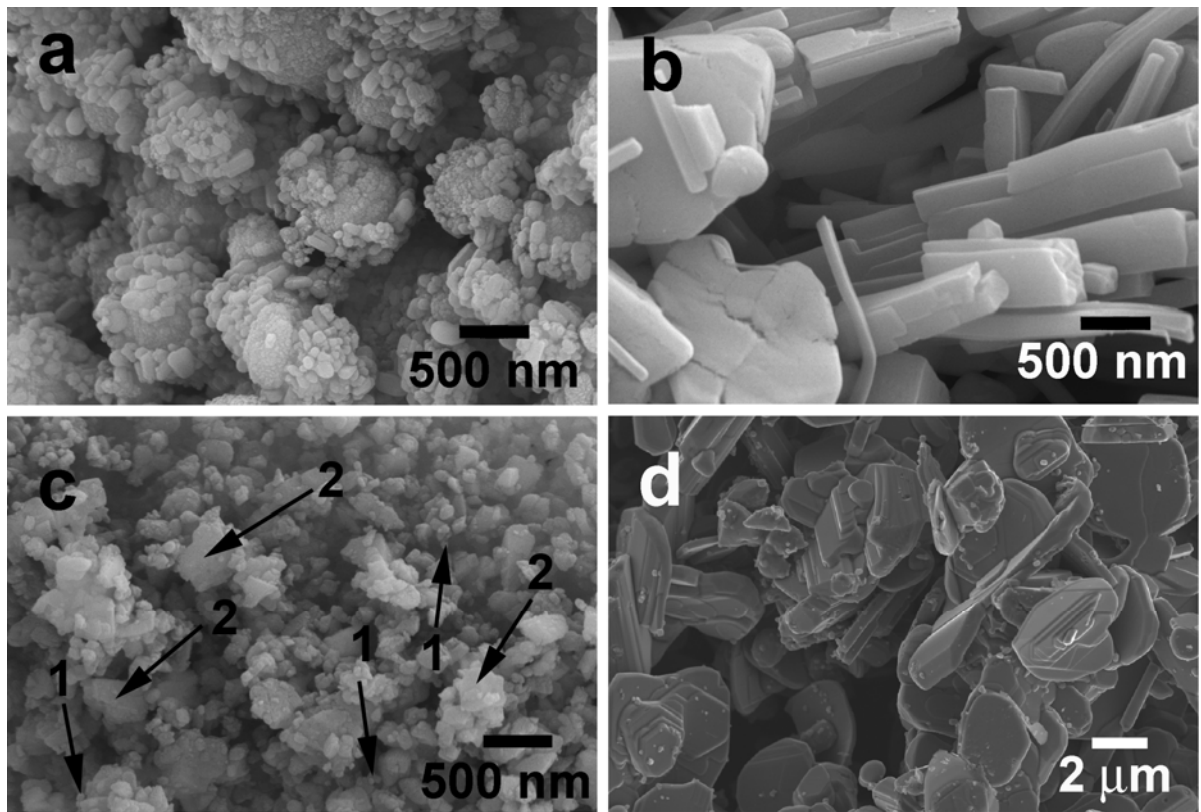


Figure 7

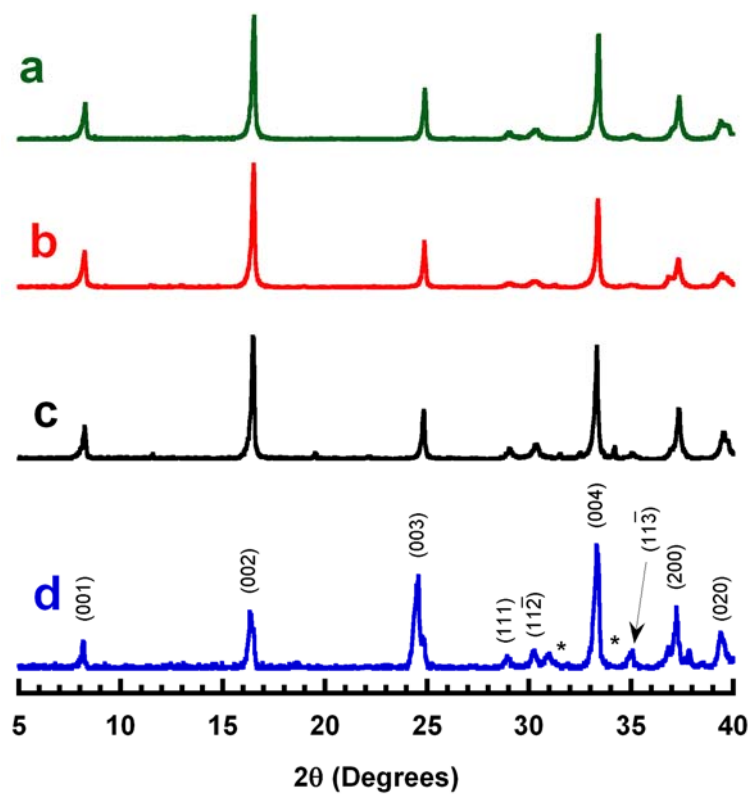


Figure 8

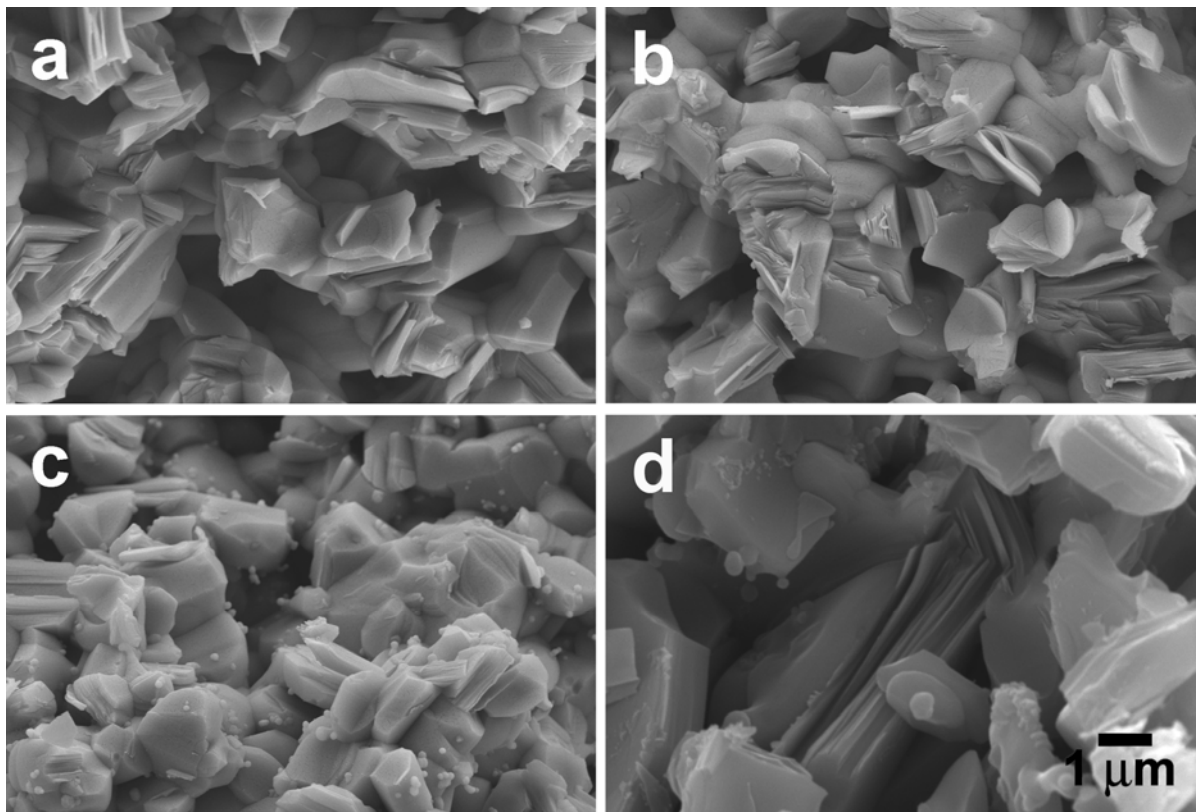


Figure 9

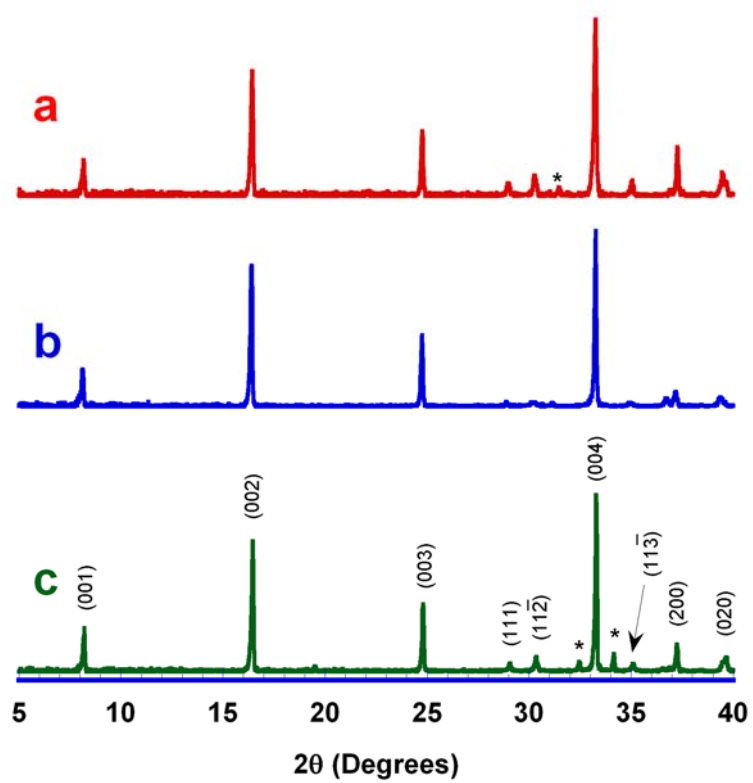


Figure 10

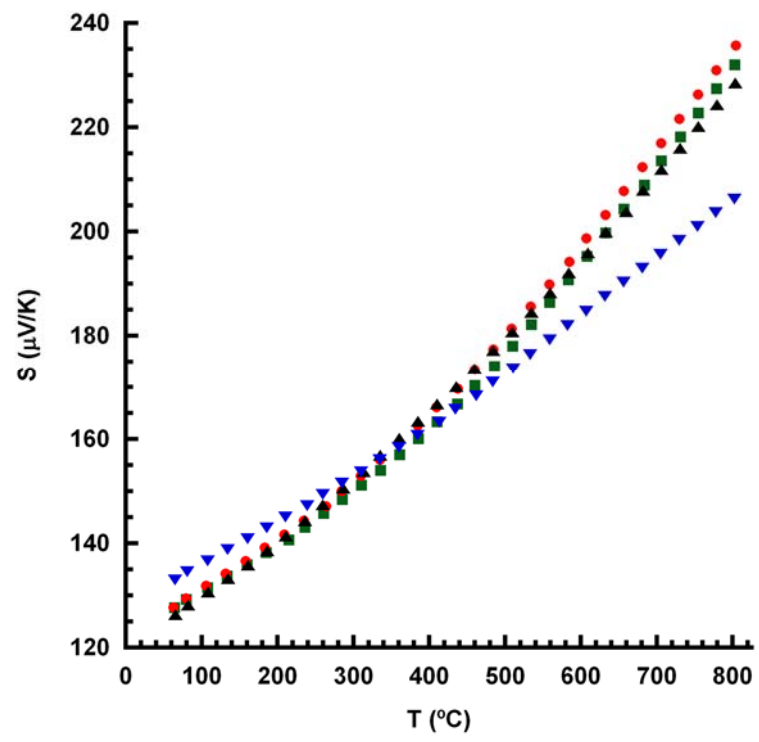


Figure 11

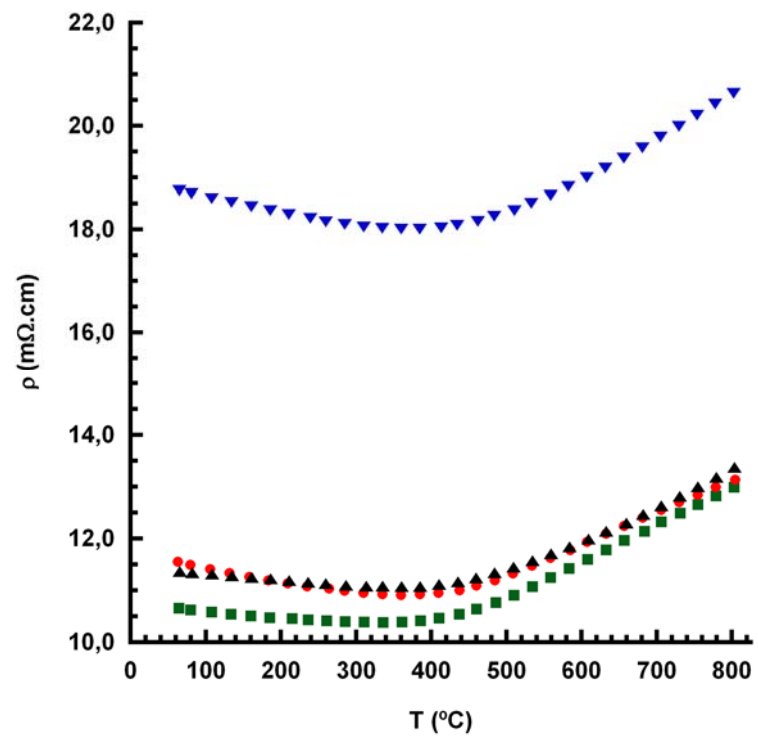


Figure 12

